Published in final edited form as:
Proc IEEE Int Symp Biomed Imaging. 2009 August 7; June 28 2009-July 1 2009: 402–405. doi:10.1109/ISBI.2009.5193069.

DETECTION PERFORMANCE ANALYSIS FOR TIME-OF-FLIGHT PET

Nannan Cao[1], **Ronald H. Huesman**[2], **William W. Moses**[2], and **Jinyi Qi**[1]

[1]Department of Biomedical Engineering, University of California at Davis, Davis, CA 95616, USA.

[2]Lawrence Berkeley National Laboratory, Berkeley, CA 94720, USA.

Abstract

In this paper, we investigate the performance of time-of-flight (TOF) PET in improving lesion detectability. We present a theoretical approach to compare lesion detectability of TOF versus non-TOF systems. Computer simulations are performed to validate the theoretical predictions. A TOF PET tomograph is simulated using the SimSET software. Images are reconstructed from list-mode data using a maximum a posteriori (MAP) method. We use a channelized Hotelling observer (CHO) to assess the detection performance. Both the receiver operating characteristic (ROC) and localization ROC (LROC) curves are compared for the TOF and non-TOF PET systems. We also study the SNR gains for TOF PET with different scatter and random fractions. Simulation results match with the theoretical predictions very well. Both results show that the TOF information improves lesion detectability and the improvement is greater with larger fractions of randoms and scatters.

Index Terms

TOF-PET; ROC; LROC; lesion detection; Channelized Hotelling observer

1. INTRODUCTION

In recent years, there has been renewed interest in the time-of-flight (TOF) positron emission tomography (PET) with the introduction of fast and efficient scintillator materials such as lutetiumoxy-orthosilicate (LSO), lutetium-yttriumoxy-orthosilicate (LYSO), and lanthanum bromide ($LaBr_3$). In TOF PET, the time difference between the detection of two coincidence photons is used to reduce the uncertainty of the annihilation positions. With a timing resolution Δt, where Δt denotes the full-width-at-half-maximum (FWHM) value, the localization uncertainty along a line of response (LOR) is reduced from the length of the LOR to $\Delta d = c\Delta t/2$, where c denotes the speed of light. Thus, TOF PET can achieve noise reduction without increasing the number of events (i.e., dose or imaging time). Early work of Snyder et al. [1] showed that for a uniform cylinder with a diameter D and a back-projection reconstruction algorithm, the SNR gain of TOF PET over non-TOF PET is given by $\sqrt{D/\Delta d}$. The formula predicts that the SNR gain is bigger for larger objects. More recently, Harrison et al. [2] showed using Monte Carlo simulations that the SNR improves with TOF but the improvement is less than theoretically predicted. Karp et al. [3] showed using both phantom and clinical measurements on a Philips Gemini TF PET/CT scanner that TOF PET provides improved contrast recovery versus noise trade-off as well as faster convergence of contrast recovery in hot lesions. Kimdom et al. [4] studied the effect of random and scatter fraction in the variance reduction of TOF PET using a simple scatter model, and they showed that TOF gain increases with higher fraction of scatters and randoms. Conti [5] theoretically modified the traditional estimate for the SNR gain by incorporating the random fraction.

In this paper, we present a theoretical approach to evaluate the performance of TOF PET in lesion detectability. We considered detection of a known lesion in a fixed background and assessed the detection performance by using a channelized Hotelling observer (CHO). A theoretical expression of the SNR of the CHO is presented and used to study the SNR gains for TOF PET with different scatter and random fractions. Computer simulations were performed to validate the theoretical predictions. We used the Monte Carlo simulation package SimSET (Simulation System for Emission Tomography) to model a TOF PET tomograph [6]. Images were reconstructed using a list-mode maximum a posteriori (MAP) method. Both the receiver operating characteristic (ROC) and localization ROC (LROC) curves are compared for the TOF and non-TOF cases.

In [7], Surti and Karp reported their experimental evaluation of a simple lesion detection task with a Philips Gemini TF PET/CT using a non-prewhitening matched filter and a list-mode OSEM reconstruction method. Comparing with their work, our work focuses on the theoretical framework for evaluating the lesion detection performance for TOF PET. In addition, we use Monte Carlo simulation to quantify the effect of randoms and scatters on the TOF detectability improvement.

This paper is organized as follows. In Section 2, we describe the system model and the Bayesian framework we used for image reconstruction. In Section 3, we present methods for lesion detection using the CHO and the theoretical expression of the SNR of CHO. Computer simulations and results are given in Section 4 to show the advantage of TOF in lesion detection. Conclusions are drawn in Section 5.

2. SYSTEM MODEL AND IMAGE RECONSTRUCTION

PET data are modelled as a set of independent Poisson random variables where the expectation of the measurements, $\bar{\boldsymbol{y}}$, relates to the unknown tracer distribution $\boldsymbol{x}$ through an affine transformation

$$\bar{\boldsymbol{y}}=E[\boldsymbol{y}|\boldsymbol{x}]=P\boldsymbol{x}+\boldsymbol{r}, \tag{1}$$

where $\boldsymbol{y}$ is the measured sinogram data, P the system matrix, and $\boldsymbol{r}$ the expectation of the background data (scatters and randoms). In our work, the elements in P for the TOF case is computed using the solid angle formulation and the ray-tracing technique that were proposed in [8], but modified by a Gaussian TOF kernel

$$g(s)=\frac{1}{\sqrt{2\pi}\sigma}\exp\left(-\frac{s^2}{2\sigma^2}\right), \tag{2}$$

where $\sigma=\Delta d/(2\sqrt{2\ln 2})$ and Δd is the FWHM value of the localization uncertainty.

We reconstruct images using the maximum a posteriori (MAP) criterion with a Gibbs prior. The MAP estimate is given by

$$\widehat{\boldsymbol{x}}(\boldsymbol{y})=\arg\max_{\boldsymbol{x}\geq 0}[L(\boldsymbol{y}|\boldsymbol{x})-\beta\phi(\boldsymbol{x})], \tag{3}$$

where $L(\boldsymbol{y}|\boldsymbol{x}) = \log p(\boldsymbol{y}|\boldsymbol{x}) = \Sigma_i(y_i \log \bar{y}_i - \bar{y}_i - \log y_i!)$ is the log-likelihood, $\phi(\boldsymbol{x})$ the prior energy function, and β the regularization parameter controlling the resolution of the reconstructed

image. We used a log-quadratic prior with $\phi(\boldsymbol{x})=\frac{1}{2}\boldsymbol{x}' R\boldsymbol{x}$, where R is a positive semi-definite matrix.

3. DETECTION PERFORMANCE ANALYSIS

3.1. Channelized Hotelling Observer

For a given reconstructed image $\boldsymbol{x}$^, a linear numerical observer computes a test statistic η ($\boldsymbol{x}$^) by

$$\eta(\widehat{\boldsymbol{x}})=\boldsymbol{t}'\widehat{\boldsymbol{x}}, \tag{4}$$

where $\boldsymbol{t}$ is the observer template. A decision whether the image contains a lesion is made by comparing η($\boldsymbol{x}$^) with a threshold. A plot of the true positive (TP) rate versus false positive (FP) rate by varying the threshold is called an ROC curve. One figure of merit for the detection performance is the area under the ROC curve (AUC).

In our work, we use the channelized Hotelling observer (CHO) which has been shown to have a good correlation with human performances [9]. The test statistic of the CHO is

$$\eta_{\mathrm{CHO}}(\widehat{\boldsymbol{x}})=\boldsymbol{z}'U'K^{-1}(U\widehat{\boldsymbol{x}}+\boldsymbol{n}), \tag{5}$$

where $\boldsymbol{z} = E[\boldsymbol{x}^|H_1] - E[\boldsymbol{x}^|H_0]$ represents the expected profile of the reconstructed lesion with H_0 being the null hypothesis representing lesion absent and H_1 the alternative hypothesis representing lesion present. The term U denotes frequency-selective channels thatmimic the human visual system, $\boldsymbol{n}$ the internal channel noise that models the uncertainty in the human detection process, and K the covariance of the channel outputs. If we assume that $\boldsymbol{n}$ is zero-mean Gaussian with a covariance matrix K_N, K can be expressed as

$$K=\frac{1}{2}U\left(\Sigma_{\widehat{\boldsymbol{x}}|H_1}+\Sigma_{\widehat{\boldsymbol{x}}|H_0}\right)U'+K_N, \tag{6}$$

where $\Sigma_{\boldsymbol{x}^|H_1}$ and $\Sigma_{\boldsymbol{x}^|H_0}$ denote the covariance matrices of $\boldsymbol{x}$^ under H_1 and H_0, respectively. In this paper, we used the differences of four Gaussian (DOG) functions with standard deviations σ = 2.653, 1.592, 0.995, 0.573 as our channel function [10]. The SNR of the CHO is given as

$$\mathrm{SNR}^2[\eta_{\mathrm{CHO}}]=\boldsymbol{z}'U'K^{-1}Uz. \tag{7}$$

When $\eta_{\mathrm{CHO}}(\boldsymbol{x}^)$ is normally distributed, the AUC is related to the SNR by

$\mathrm{AUC}=\frac{1}{2}\left[1+\mathrm{erf}\left(\frac{\mathrm{SNR}}{2}\right)\right]$, where $\mathrm{erf}(x)=2\int_0^x e^{-t^2}dt/\sqrt{\pi}$ is the error function.

3.2. Lesion Detectability in MAP Reconstruction

Assuming that the presence of a small lesion has little effect on the Poisson noise in the data, it was derived in [11] that for the special case where the signal is known exactly (SKE), the theoretical expression of SNR for the CHO can be approximated as

$$\mathrm{SNR}^2[\eta(\widehat{x})]=\boldsymbol{w}' B^{-1}\boldsymbol{w}, \tag{8}$$

where

$$B=\tilde{U}\,\mathrm{diag}\left[\frac{\lambda_i}{(\lambda_i+\beta\mu_i)^2}\right]\tilde{U}'+K_N, \tag{9}$$

and $\boldsymbol{w}$ is a column vector with its kth element defined as

$$w_k=\sum_i \frac{\tilde{U}_k\lambda_i\xi_i}{\lambda_i+\beta\mu_i}. \tag{10}$$

$\{\lambda_i, i = 1, \ldots,N\}$ and $\{\mu_i, i = 1, \ldots,N\}$ are the Fourier coefficients of the column vector corresponding to the lesion location of F and R, respectively, where $F = P'$ diag$[1/y_i]P$ is the Fisher information matrix. $\tilde{U}$ are the Fourier coefficients of the channel functions, and ξ_i the Fourier transform of the expected lesion profile. More details on the computation of λ_i and μ_i can be found in [12].

Eq. (8) allows fast evaluation of lesion detectability under varies conditions because there is no image reconstruction involved. The theoretical expression shows that the TOF gain in lesion detectability depends on prior parameters (β and μ_i) and channel noise. When $\beta = 0$ and $K_N = 0$, the TOF gain in SNR^2 is proportional to the size of the background object.

4. COMPUTER SIMULATIONS

We used the Monte Carlo simulation package SimSET to model a TOF PET Tomograph that is similar to the one under development at Lawrence Berkeley National Laboratory. The detector ring has a diameter of 79.5 cm. It consists of 384 crystals of size $6.15\times100\times25\mathrm{mm}^3$. We set the axial length to be 10 cm to increase sensitivity. The timing resolution is 200 ps, which corresponds to a full-width-half-maximum (FWHM) of 3 cm. The coincidence window is selected as 3 ns. Timing difference of each coincidence event is discretized into 127 timing bins with a width of 7.5 mm.

We used a 10-cm long elliptical cylinder with uniform activity as the background (Fig. 1). The cylinder has a long axis of 30 cm and a short axis of 20 cm. A hot rod of 12 mm in diameter is placed at the center of the phantom as a lesion. The lesion-to-background activity ratio is 3 : 2. The true and scatter coincidences were generated by SimSET directly with an energy window between 400 keV and 600 keV. For random coincidences, we first calculated their expectations from singles rate that were obtained by running the SimSET in SPECT mode and then generated each random coincidence as a Poisson realization. Each random coincidence was assigned a time difference that is uniformly distributed among the 127 time bins. We generated 80 independent noisy data sets with an average of 1.06M prompt events in each data set. The random fraction (RF = R/(T + S + R)) is around 24.5% and the scatter fraction (SF = S/(T + S)) is around 27.8%. All images were reconstructed from list-mode data using the MAP algorithm with 248×248 $3\times3\times100$ mm^3 voxels.

Fig. 2 shows reconstructed images with and without TOF information and the corresponding horizontal profile through the center. In comparison, the non-TOF image is much noisier than

the TOF reconstruction. The hot spot can hardly be seen in the non-TOF image, but is clearly visible in the TOF image.

Fig. 3(a) shows a comparison of the ROC curves obtained from the Monte Carlo reconstructions ($\beta = 2.5\times10^{-13}$). We can see that the TOF PET (AUC = 0.9718) clearly outperforms the non-TOF PET (AUC = 0.8770) in terms of lesion detection. We also evaluate the localization performance by applying the CHO to multiple non-overlapping regions in the images and plotted the LROC curves in Fig. 3(b). The TP rate in the LROC curve is the joint probability of detecting and correctly localizing the lesion in the images [13]. The TOF PET has an area of 0.6719 under the LROC curve, whereas non-TOF PET only has 0.4370. Furthermore, the probability of correctly localizing the lesion with the TOF PET is 80%, whereas with the non-TOF PET it is around 60%.

One advantage of using computer simulations is that we can separate true, scattered, and random events, and study their effect on TOF gain separately. In Fig. 4, we show the measured and theoretically predicated SNRs for MAP reconstructions with different β values under three different conditions: true events only, true plus scattered events, and all prompt events. We can see that the measured SNRs match well with the theoretical predications for all three cases. The measured SNR gains are given in Table 1, which show that the SNR gain is a function of the regularization parameter β. For the current configuration, the maximum SNR for both TOF and non-TOF occurs at $\beta = 2.5 \times 10^{-12}$, and the gain of the maximum SNR is around 1.8067. The gain is also greater when scatters and randoms are considered, which is consistent with the results in [4].

5. CONCLUSIONS

In this paper, we present a theoretical approach to investigate the performance of TOF PET in improving the lesion detectability. We used the list-mode MAP reconstruction and assessed the detection performance using CHO. We showed that the TOF PET has better lesion detection performance than the non-TOF PET. We found that the TOF gain is a function of the regularization parameter used in image reconstruction and is greater when scatters and randoms are included. The theoretical predictions match well with computer simulation results.

The theoretical expression provides us a fast approach to evaluate the lesion detection performance of TOF PET. In future work, we plan to use the theoretical expression to investigate the performance of TOF PET for different lesion and background configurations. We also plan to examine the effect of different timing kernels on the detection performance.

Acknowledgments

This work is supported in part by the Director, Office of Science, Office of Biological and Environmental Research, Medical Science Division of the U.S. Department of Energy under Contract No. DE-AC02-05CH11231, and in part by the National Institutes of Health, National Institute of Biomedical Imaging and Bioengineering under grant number R01-EB006085.

6. REFERENCES

1. Synder D, Thomas LJ, Ter-Pogossian M. A mathematical model for positron-emission tomography systems having time-of-flight measurements. IEEE Tran. Nucl. Sci 1981;vol. 28:3575–3583.
2. Harrison, R.; Alessio, A.; Kinahan, P.; Lewellen, T. Signal to noise ratio in simulations of time-of-flight positron emission tomography; Conf. Record of the 2004 Nucl. Sci. Symp. and Med. Imaging Conf; 2004. p. 4080-4083.
3. Karp J, Surti S, Daube-Witherspoon M, Muehllehner G. Benefit of time-of-flight in PET: Experimental and clinical results. J. Nucl. Med 2008;vol. 49:462–470. [PubMed: 18287269]

4. Kimdom, J.; Qi, J.; Moses, WW. Effect of random and scatter fractions in variance reduction using time-of-flight information; Conf. Record of the 2004 Nucl. Sci. Symp. and Med. Imaging Conf; 2004. p. 2571-2573.

5. Conti M. Effect of randoms on signal-to-noise-ratio in TOF PET. IEEE Tran. Nucl. Sci 2006;vol. 53:1188–1193.

6. Lewellen, TK.; Harrison, RL.; Vannoy, S. The SimSET program, Monte Carlo Calculations in Nuclear Medicine. Ljungberg, M.; Strand, S-E.; King, MA., editors. Philadelphia, PA: Inst. Phys.; 1998.

7. Surti S, Karp J. Experimental evaluation of a simple lesion detection task with time-of-flight pet. Phys. Med. Biol 2009;vol. 54:373–384. [PubMed: 19098351]

8. Huesman RH, Klein G, Moses W, Qi J, Reutter B, Virador P. List-mode maximum-likelihood reconstruction applied to positron emission mammography (PET) with irregular sampling. IEEE Tran. Med. Imaging 2000;vol. 19:532–537.

9. Yao, J.; Barrett, HH. Predicting human performance by a channelized hotelling model; Proc. SPIE; 1992. p. 161-168.

10. Oldan J, Kulkarni S, Xing Y, Khurd P, Gindi G. Channelized hotelling and human observer study of optimal smoothing in spect map reconstruction. IEEE Tran. Nucl. Sci 2004;vol. 51:733–741.

11. Qi J. Analysis of lesion detectability in bayesian emission reconstruction with nonstationary object variability. IEEE Trans. Med. Imaging 2004;vol. 23:321–329. [PubMed: 15027525]

12. Qi J, Leahy RM. Resolution and noise properties of map reconstruction for fully 3d pet. IEEE Tran. Med. Imaging 2000;vol. 19:493–506.

13. Swensson R. Unified measurement of observer performance in detecting and localizing target objects on images. Med. Phys 1996;vol. 23:1709–1725. [PubMed: 8946368]

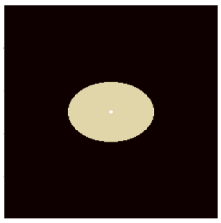

Fig. 1.
Illustration of the phantom used in the simulation.

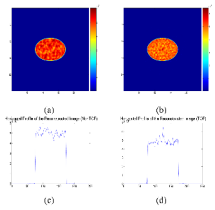

Fig. 2.
Reconstructed images using MAP with $\beta = 2.5 \times 10^{-13}$. (a) Non-TOF reconstruction. (b) TOF reconstruction. (c) Horizontal profile through the central line of (a). (d) Horizontal profile through the central line of (b).

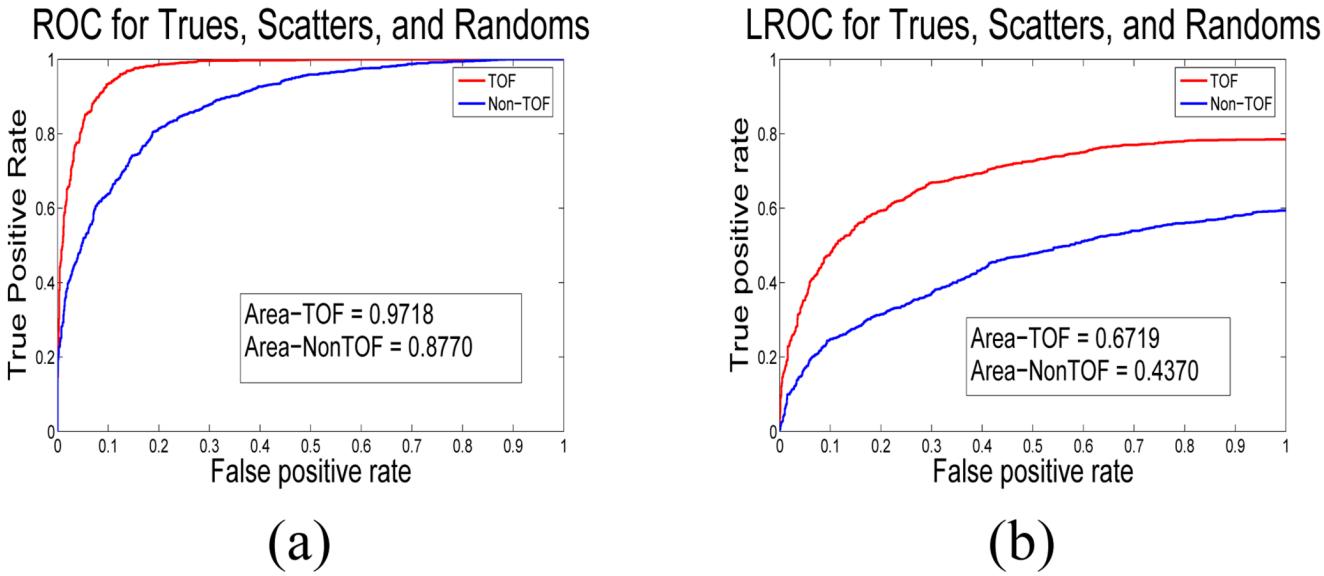

Fig. 3.
ROC and LROC curves for TOF and non-TOF reconstructions with $\beta = 2.5 \times 10^{-13}$.

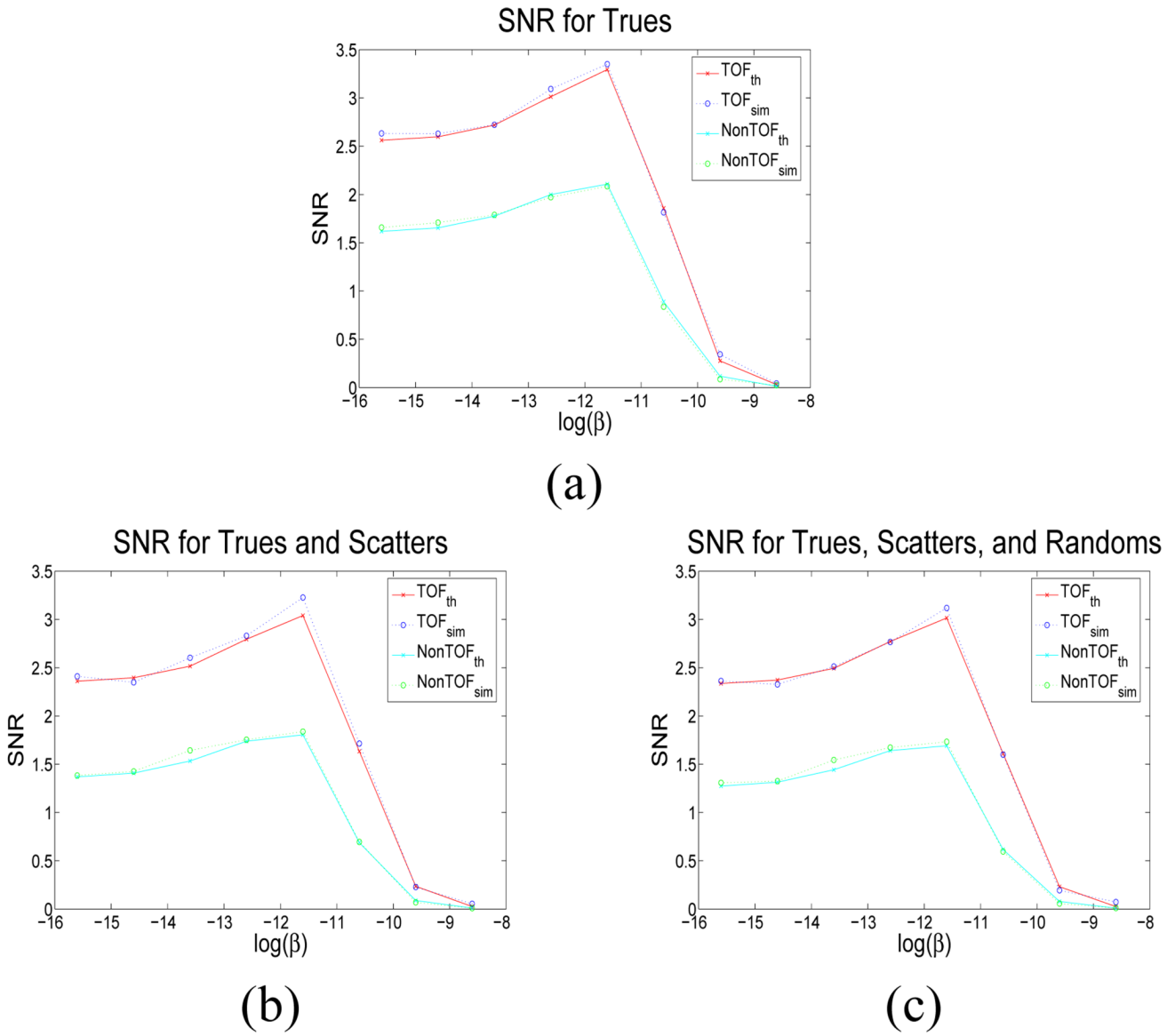

Fig. 4.
Theoretically predicted and measured SNRs for MAP reconstruction with different β values under three conditions. (a) Only trues are considered. (b) Only trues and scatters are considered. (c) All prompts (trues, scatters, and randoms) are considered.

Table 1

Measured SNR Gains ($SNR_{TOF}/SNR_{non-TOF}$) as a function of β.

β (2.5×)	10^{-16}	10^{-15}	10^{-14}	10^{-13}	10^{-12}
T	1.6068	1.5689	1.5221	1.5397	1.5886
T + S	1.7561	1.6131	1.5836	1.6473	1.7432
T + S + R	1.8005	1.6540	1.6267	1.7559	1.8067